Supporting Information for Chromophores in Molecular Nanorings: When is a Ring a Ring?

Patrick Parkinson,*,† Dmitry V Kondratuk,‡ Christopher Menelaou,† Juliane Q Gong,† Harry L Anderson,‡ and Laura M Herz*,†

Department of Physics, University of Oxford, Clarendon Laboratory, Parks Road, Oxford OX1 3PU, United Kingdom, and Department of Chemistry, University of Oxford, Chemistry Research Laboratory, Oxford OX1 3TA, United Kingdom

E-mail: p.parkinson1@physics.ox.ac.uk; l.herz1@physics.ox.ac.uk

---

*To whom correspondence should be addressed

†Oxford Physics

‡Oxford Chemistry

Contents

S1 Synthesis of long linear porphyrin oligomers

S1.1 General Methods

All reagents were purchased from commercial sources and solvents were use as supplied unless otherwise noted. Dry solvents ($CHCl_3$, CH_2Cl_2 and toluene) were obtained by passing through alumina under N_2. Diisopropylamine was dried over calcium hydride, distilled and stored under N_2 over molecular sieves. NMR data were collected at 500 MHz using a Bruker AVII500 (with cryoprobe) or DRX500 or at 400 MHz using a Bruker AVII400 or AVIII400 at 298 K. Chemical shifts are quoted as parts per million (ppm) relative to residual $CHCl_3$ (at δ 7.27 ppm for ^1H NMR) and coupling constants (J) are reported in Hertz. MALDI-

ToF spectra were measured at the EPSRC National Mass Spectrometry service (Swansea) using the Applied Biosystems Voyager DE-STR. UV-vis-NIR absorbance measurements were recorded at 25 °C with a Perkin-Elmer Lambda 20 photospectrometer using quartz 1 cm cuvettes. Size exclusion chromatography (SEC) was carried out using Bio-Beads SX1, 200–400 mesh (Bio Rad). Analytical and semi-preparative GPC was carried out on Shimadzu Recycling GPC system equipped with LC-20 AD pump, SPD-M20A UV detector and a set of JAIGEL 3H (20 x 600 mm) and JAIGEL 4H (20 x 600 mm) columns in toluene/1% pyridine as eluent with a flow rate of 3.5 mL/min.

S1.2 Synthetic Procedures

S1.2.1 Synthesis of Known Compounds

Porphyrin monomer ***l*-P1**$_{\mathrm{H,THS}}$[S1] and ***l*-P8**[S2] were prepared using previously reported procedures.

S1.2.2 Synthesis of Novel Compounds

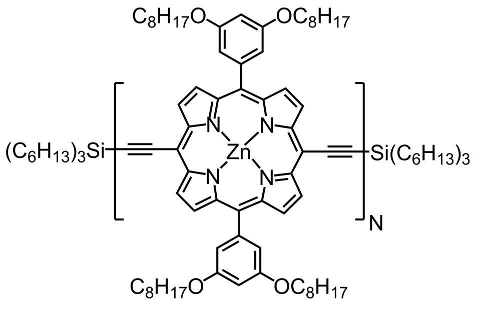

***l*-P8** (*N* = 8)
***l*-P10** (*N* = 10)
***l*-P18** (*N* = 18)
***l*-P26** (*N* = 26)
***l*-P34** (*N* = 34)
***l*-P42** (*N* = 42)
***l*-P50** (*N* = 50)

- Zinc 5,15-Bis-(3,5-bis-octyloxy-phenyl)-10,20-trihexylsilanylethynyl-porphyrin 10-mer *l*-P10
- Zinc 5,15-Bis-(3,5-bis-octyloxy-phenyl)-10,20-trihexylsilanylethynyl-porphyrin 18-mer *l*-P18

- Zinc 5,15-Bis-(3,5-bis-octyloxy-phenyl)-10,20-trihexylsilanylethynyl-porphyrin 26-mer *l*-P26

- Zinc 5,15-Bis-(3,5-bis-octyloxy-phenyl)-10,20-trihexylsilanylethynyl-porphyrin 34-mer *l*-P34

- Zinc 5,15-Bis-(3,5-bis-octyloxy-phenyl)-10,20-trihexylsilanylethynyl-porphyrin 42-mer *l*-P42

- Zinc 5,15-Bis-(3,5-bis-octyloxy-phenyl)-10,20-trihexylsilanylethynyl-porphyrin 50-mer *l*-P50

Fully-protected linear porphyrin 8-mer ***l*-P8** (130.0 mg, 14.1 μmol) was dissolved in CH_2Cl_2 (30.0 mL) and pyridine (0.3 mL) and the solution degassed. Tetra-n-butylammonium fluoride (1.0 M in THF, 140 μL, 0.14 mmol) was added and the reaction mixture stirred at 20 °C for 15 minutes under N_2 atmosphere. The reaction was quenched with MeOH (10 mL), stirred and the precipitate of deprotected ***l*-P8**$_{\mathrm{H,H}}$ filtered off and dried in high vacuum. This ***l*-P8**$_{\mathrm{H,H}}$ was added to half-deprotected porphyrin monomer **P1**$_{\mathrm{H,Si}}$ (77.0 mg, 0.056 mmol) dissolved in $CHCl_3$ (130 mL) and pyridine (1.3 mL). A catalyst solution was prepared by dissolving dichlorobis(triphenylphosphine)-palladium(II) (10 mg, 0.14 mmol), copper(I) iodide (11.0 mg, 0.0577 mmol) and 1,4-benzoquinone (30 mg, 0.277 mmol) in the mixture of $CHCl_3$ (7.0 mL) and freshly distilled i-Pr_2NH (350 μL). All the catalysts solution was added to the solution of ***l*-P8**$_{\mathrm{H,H}}$ and **P1**$_{\mathrm{H,Si}}$. The reaction mixture was stirred at 20 °C overnight, after which GPC analysis of the reaction mixture confirmed that all starting material was consumed. Excess of **P1**$_{\mathrm{H,Si}}$ (350 mg, 0.256 mmol) was added and 35 mL of the fresh catalysts solution prepared as above and added. The reaction mixture was stirred at 20 °C for 3 h, after which the reaction mixture was passed through short silica column ($CHCl_3$/1% pyridine), then solvents removed, and the residue purified by a size exclusion column on Biobeads SX-1 ($CHCl_3$/1% pyridine) to remove the 1,4-benzoquinone. Recycling GPC on preparative JAIGEL columns (toluene/1% pyridine) yielded ***l*-P2** (400 mg 94% vs. **P1**$_{\mathrm{H,Si}}$),

***l*-P10** (33.0 mg 20.5% vs. ***l*-P8**), ***l*-P18** (27.0 mg 19.1% vs. ***l*-P8**), ***l*-P26** (15.0 mg 11.1% vs. ***l*-P8**), ***l*-P34** (12.8 mg 9.7% vs. ***l*-P8**), ***l*-P42** (6.6 mg 5.1% vs. ***l*-P8**) and ***l*-P50** (2.0 mg 1.6% vs. ***l*-P8**) as brown solids.

***l*-P2** ^{1}H NMR (400 MHz, $CDCl_3$/1% d_5-pyridine): δ_H 0.93-1.01 (m, 42H, -CH_3), 1.03-1.17 (m, 12H, -CH_2), 1.35-1.67 (m, 116H, -CH_2), 1.82-1.98 (m, 28H, -CH_2), 4.20 (t, 16H, J = 6.5 Hz, -OCH_2), 6.93 (s, 4H, -ArH_{para}), 7.43 (d, 8H, J = 2.0 Hz, -ArH_{ortho}), 9.06 (d, 4H, J = 4.5 Hz, -ArH_β), 9.17 (d, 4H, J = 4.5 Hz, -ArH_β), 9.74 (d, 4H, J = 4.5 Hz, -ArH_β), 9.98 (d, 4H, J = 4.5 Hz, -ArH_β). As Reference 1.

***l*-P10** ^{1}H NMR (400 MHz, $CDCl_3$/1% d_5-pyridine): δ_H 0.66-0.74 (m, 138H, -CH_3), 0.85-0.89 (m, 12H, -CH_2), 1.07-1.42 (m, 424H, -CH_2), 1.59-1.64 (m, 12H, -CH_2), 1.67-1.76 (m, 92H, -CH_2), 3.99 (m, 80H, -OCH_2), 6.77-6.80 (m, 20H, -ArH_{para}), 7.21-7.28 (m, 40H, -ArH_{ortho}), 8.84 (d, 4H, J = 4.4 Hz, -ArH_β), 8.93-8.96 (m, 36H, -ArH_β), 9.54 (d, 4H, J = 4.5 Hz, -ArH_β), 9.73-9.77 (m, 36H, -ArH_β). As Reference 2.

***l*-P18** ^{1}H NMR (400 MHz, $CDCl_3$/1% d_5-pyridine): δ_H 0.60-0.70 (m, 234H, -CH_3), 0.80-0.85 (m, 12H, -CH_2), 0.99-1.35 (m, 774H, -CH_2), 1.55-1.61 (m, 12H, -CH_2), 1.64-1.71 (m, 156H, -CH_2), 3.94 (m, 144H, -OCH_2), 6.75-6.77 (m, 36H, -ArH_{para}), 7.17-7.23 (m, 72H, -ArH_{ortho}), 8.81 (d, 4H, J = 4.5 Hz, -ArH_β), 8.89-8.93 (m, 68H, -ArH_β), 9.51 (d, 4H, J = 4.5 Hz, -ArH_β), 9.70-9.74 (m, 68H, -ArH_β). As Reference 2.

***l*-P26** ^{1}H NMR (400 MHz, $CDCl_3$/1% d_5-pyridine): δ_H 0.84-0.93 (m, 330H, -CH_3), 1.00-1.05 (m, 12H, -CH_2), 1.10-1.61 (m, 1064H, -CH_2), 1.74-1.80 (m, 12H, -CH_2), 1.87-1.97 (m, 220H, -CH_2), 4.19 (m, 208H, -OCH_2), 6.90-6.96 (m, 52H, -ArH_{para}), 7.37-7.45 (m, 104H, -ArH_{ortho}), 8.96 (d, 4H, J = 4.6 Hz, -ArH_β), 9.06-9.11 (m, 100H, -ArH_β), 9.64 (d, 4H, J = 4.6 Hz, -ArH_β), 9.87-9.93 (m, 100H, -ArH_β); m/z (MALDI ToF) 28783 ($C_{1804}H_{2210}N_{104}O_{104}Si_2Zn_{26}$, M^+ requires 28771.54). λ_{max} ($CHCl_3$/1% pyridine) / nm 473, 593, 817.

_l_-P34 ^{1}H NMR (400 MHz, CDCl$_3$/1% d_5-pyridine): δ_H 0.82-0.93 (m, 426H, -CH_3), 1.00-1.05 (m, 12H, -CH_2), 1.15-1.63 (m, 1384H, -CH_2), 1.74-1.80 (m, 12H, -CH_2), 1.84-1.99 (m, 284H, -CH_2), 4.19 (m, 272H, -OCH_2), 6.89-6.96 (m, 68H, -ArH_{para}), 7.36-7.46 (m, 136H, -ArH_{ortho}), 8.96 (d, 4H, J = 4.6 Hz, -ArH_β), 9.06-9.12 (m, 132H, -ArH_β), 9.64 (d, 4H, J = 4.6 Hz, -ArH_β), 9.87-9.94 (m, 132H, -ArH_β); m/z (MALDI ToF) 37501 ($C_{2348}H_{2866}N_{136}O_{136}Si_2Zn_{34}$, M$^+$ requires 37449.80). λ_{max} (CHCl$_3$/1% pyridine) / nm 473, 593, 818.

_l_-P42 ^{1}H NMR (400 MHz, CDCl$_3$/1% d_5-pyridine): δ_H 0.82-0.93 (m, 522H, -CH_3), 1.00-1.05 (m, 12H, -CH_2), 1.15-1.63 (m, 1704H, -CH_2), 1.74-1.80 (m, 12H, -CH_2), 1.84-1.98 (m, 348H, -CH_2), 4.19 (m, 336H, -OCH_2), 6.90-6.97 (m, 84H, -ArH_{para}), 7.35-7.48 (m, 168H, -ArH_{ortho}), 8.96 (d, 4H, J = 4.6 Hz, -ArH_β), 9.04-9.14 (m, 164H, -ArH_β), 9.64 (d, 4H, J = 4.6 Hz, -ArH_β), 9.86-9.93 (m, 164H, -ArH_β); m/z (MALDI ToF) 46253 ($C_{2892}H_{3522}N_{168}O_{168}Si_2Zn_{42}$, M$^+$ requires 46128.06). λ_{max} (CHCl$_3$/1% pyridine) / nm (log ϵ) 473 (6.63), 593 (5.55), 818 (6.45).

_l_-P50 ^{1}H NMR (400 MHz, CDCl$_3$/1% d_5-pyridine): δ_H 0.76-0.94 (m, 618H, -CH_3), 1.00-1.05 (m, 12H, -CH_2), 1.15-1.63 (m, 2024H, -CH_2), 1.74-1.80 (m, 12H, -CH_2), 1.84-2.01 (m, 412H, -CH_2), 4.19 (m, 400H, -OCH_2), 6.89-6.96 (m, 100H, -ArH_{para}), 7.36-7.46 (m, 200H, -ArH_{ortho}), 8.96 (d, 4H, J = 4.6 Hz, -ArH_β), 9.04-9.13 (m, 196H, -ArH_β), 9.64 (d, 4H, J = 4.6 Hz, -ArH_β), 9.87-9.94 (m, 196H, -ArH_β); m/z (MALDI ToF) 54483.7 ($C_{3436}H_{4178}N_{200}O_{200}Si_2Zn_{50}$, M+ requires 54807.59). λ_{max} (CHCl$_3$/1% pyridine) / nm 473, 593, 819.

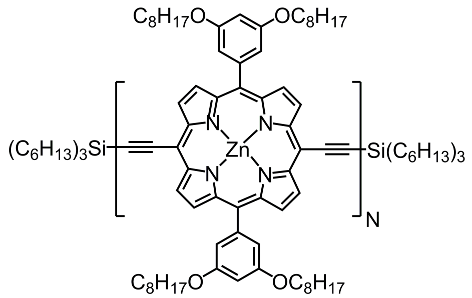

_l_-P10 (*N* = 10)
_l_-P12 (*N* = 12)
_l_-P22 (*N* = 22)
_l_-P32 (*N* = 32)

- Zinc 5,15-Bis-(3,5-bis-octyloxy-phenyl)-10,20-trihexylsilanylethynyl-porphyrin 12-mer ***l*-P12**
- Zinc 5,15-Bis-(3,5-bis-octyloxy-phenyl)-10,20-trihexylsilanylethynyl-porphyrin 22-mer ***l*-P22**
- Zinc 5,15-Bis-(3,5-bis-octyloxy-phenyl)-10,20-trihexylsilanylethynyl-porphyrin 32-mer ***l*-P32**

Fully-protected linear porphyrin 10-mer ***l*-P10** (29.4 mg, 2.6 μmol) was dissolved in CH_2Cl_2 (6.0 mL) and the solution degassed. Tetra-*n*-butylammonium fluoride (1.0 M in THF, 32 μL, 32.0 μmol) was added and the reaction mixture stirred at 20 °C for 20 minutes under N_2 atmosphere. The reaction was quenched with MeOH (10.0 mL), stirred and the precipitate of ***l*-P10**$_{\mathrm{H,H}}$ filtered off and dried in high vacuum. This ***l*-P10**$_{\mathrm{H,H}}$ was added to half-deprotected porphyrin monomer **P1**$_{\mathrm{H,Si}}$ (15.0 mg, 0.011 mmol) dissolved in $CHCl_3$ (25 mL) and pyridine (250 μL). A catalyst solution was prepared by dissolving dichlorobis(triphenylphosphine)-palladium(II) (2 mg, 2.84 μmol), copper(I) iodide (2.0 mg, 10.5 μmol) and 1,4-benzoquinone (6.0 mg, 0.056 mmol) in a mixture of $CHCl_3$ (1.4 mL) and freshly distilled *i*-Pr_2NH (70.0 μL). 1.33 mL of the catalysts solution was added to the solution of ***l*-P10**$_{\mathrm{H,H}}$ and **P1**$_{\mathrm{H,Si}}$. The reaction mixture was stirred at 20 °C for 3 h, after which GPC analysis of the reaction mixture confirmed that all starting material is consumed. Excess of **P1**$_{\mathrm{H,Si}}$ (70 mg, 0.051 mmol) was added and 7 mL of the catalysts solution prepared as above. The reaction mixture was stirred at 20 °C for 3 h, after which solvents were removed, and the residue purified by a size exclusion column on Biobeads SX-1 ($CHCl_3$/1% pyridine) to remove the 1,4-benzoquinon and catalysts. Recycling GPC on preparative JAIGEL columns (toluene/1% pyridine) yielded ***l*-P2** (50 mg 58.8% vs. **P1**$_{\mathrm{H,Si}}$), ***l*-P12** (10.4 mg 29.4% vs. ***l*-P10**), ***l*-P22** (6.7 mg 21.1% vs. ***l*-P10**) and ***l*-P32** (3.1 mg 10.1% vs. ***l*-P10**) as brown solids.

***l*-P12** ^{1}H NMR (400 MHz, $CDCl_3$/1% d_5-pyridine): δ_H 0.73-0.85 (m, 162H, -CH_3), 0.91-0.98 (m, 12H, -CH_2), 1.13-1.51 (m, 504H, -CH_2), 1.65-1.75 (m, 12H, -CH_2), 1.75-1.87 (m, 108H, -CH_2), 4.09 (m, 96H, -OCH_2), 6.83-6.90 (m, 24H, -ArH_{para}), 7.32-7.38 (m, 48H, -ArH_{ortho}), 8.89-8.91 (m, 4H, -ArH_β), 8.99-9.05 (m, 44H, -ArH_β), 9.58-9.61 (m, 4H, -ArH_β), 9.81-9.85 (m, 44H, -ArH_β); m/z (MALDI ToF) 13600 ($\mathrm{C_{852}H_{1062}N_{48}O_{48}Si_2Zn_{12}}$, M^+ requires 13585). λ_{max} ($\mathrm{CHCl_3}$/1% pyridine) / nm (log ϵ) 471 (6.15), 593 (5.04), 812 (5.91).

***l*-P22** ^{1}H NMR (400 MHz, $\mathrm{CDCl_3}$/1% d_5-pyridine): δ_H 0.67-0.80 (m, 276H, -CH_3), 0.87-0.94 (m, 12H, -CH_2), 1.09-1.47 (m, 910H, -CH_2), 1.63-1.69 (m, 12H, -CH_2), 1.72-1.81 (m, 188H, -CH_2), 4.13 (m, 176H, -OCH_2), 6.78-6.94 (m, 44H, -ArH_{para}), 7.29-7.36 (m, 88H, -ArH_{ortho}), 8.88 (d, 4H, J = 4.4 Hz, -ArH_β), 8.96-9.03 (m, 84H, -ArH_β), 9.57 (d, 4H, J = 4.4 Hz, -ArH_β), 9.76-9.85 (m, 84H, -ArH_β); m/z (MALDI-ToF) 24475 ($\mathrm{C_{1532}H_{1882}N_{88}O_{88}Si_2Zn_{22}}$, M^+ requires 24432). λ_{max} ($\mathrm{CHCl_3}$/1% pyridine) / nm (log ϵ) 471 (6.40), 593 (5.29), 814 (6.20).

***l*-P32** ^{1}H NMR (400 MHz, $\mathrm{CDCl_3}$/1% d_5-pyridine): δ_H 0.65-0.74 (m, 396H, -$\mathrm{CH_3}$), 0.84-0.91 (m, 12H, -CH_2), 1.04-1.43 (m, 1310H, -CH_2), 1.57-1.66 (m, 12H, -CH_2), 1.67-1.79 (m, 268H, -CH_2), 3.86-4.16 (m, 256H, -OCH_2), 6.75-6.83 (m, 64H, -ArH_{para}), 7.21-7.29 (m, 128H, -ArH_{ortho}), 8.85 (d, 4H, J = 4.4 Hz, -ArH_β), 8.93-8.98 (m, 124H, -ArH_β), 9.54 (d, 4H, J = 4.4 Hz, -ArH_β), 9.74-9.79 (m, 124H, -ArH_β); m/z (MALDI-ToF) 35372 ($\mathrm{C_{2212}H_{2702}N_{128}O_{128}Si_2Zn_{32}}$, M^+ requires 35280). λ_{max} ($\mathrm{CHCl_3}$/1% pyridine) / nm (log ϵ) 471 (6.54), 593 (5.44), 818 (6.36).

S1.3 Characterisation of Linear Oligomers

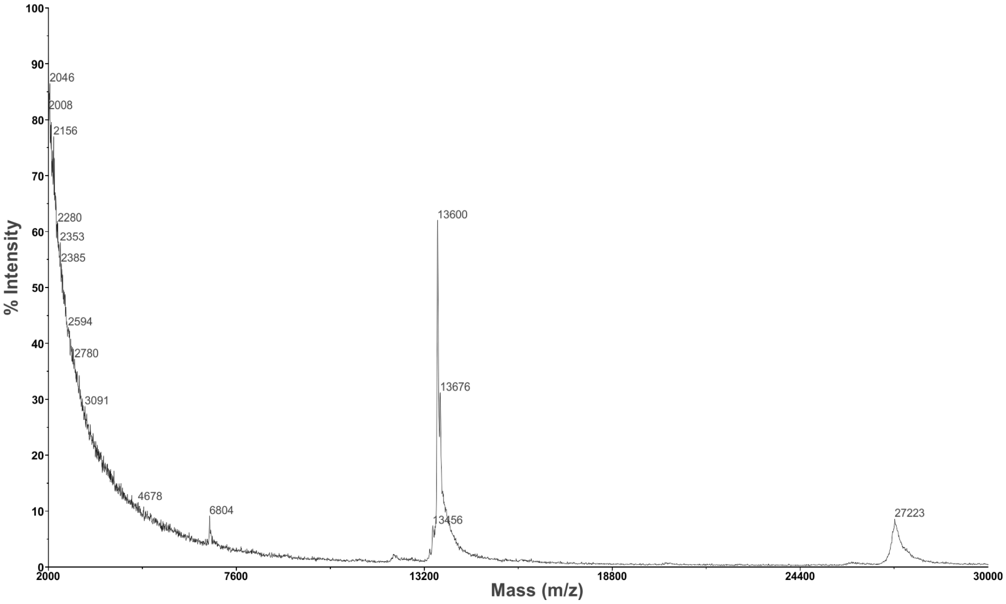

Figure S1: MALDI-ToF analysis of **_l_-P12**. The major peak corresponds to **_l_-P12** (m/z 13600, expected 13585). DCTB was used as matrix.

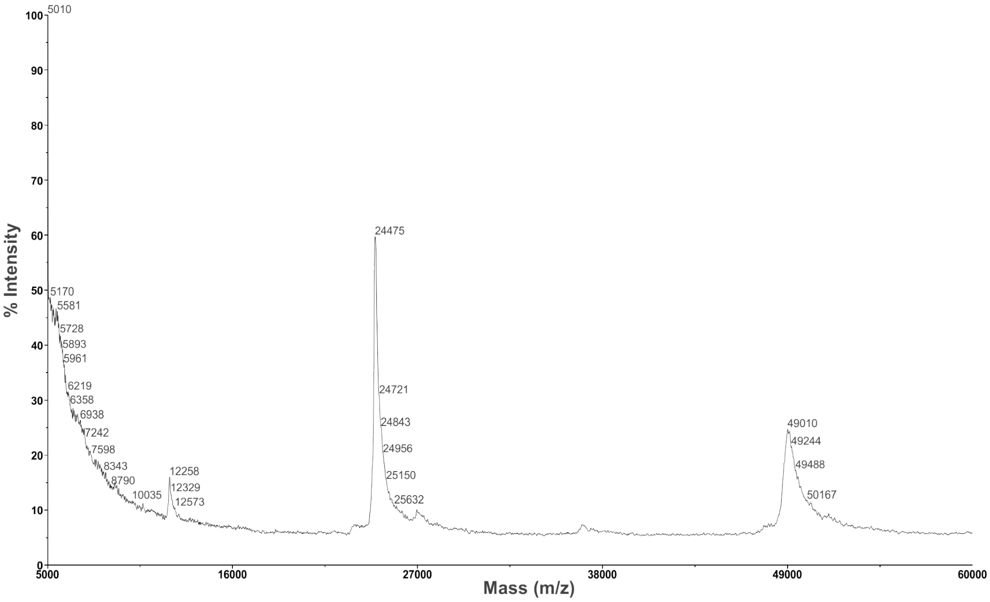

Figure S2: MALDI-ToF analysis of **_l_-P22**. The major peak corresponds to **_l_-P22** (m/z 24475, expected 24432). DCTB was used as matrix.

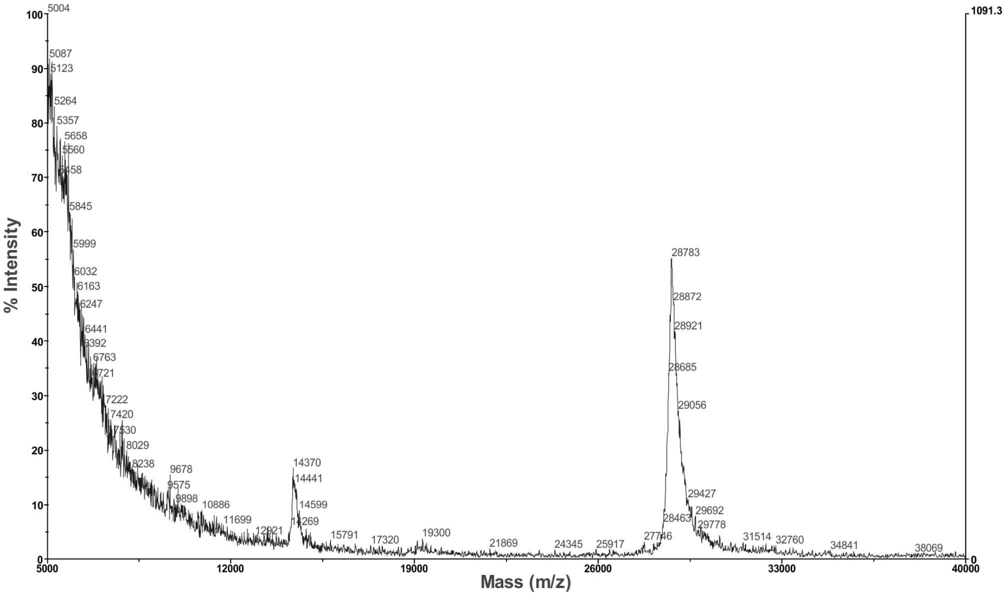

Figure S3: MALDI-ToF analysis of ***l*-P26**. The major peak corresponds to ***l*-P26** (m/z 28783, expected 28771.54). DCTB was used as matrix.

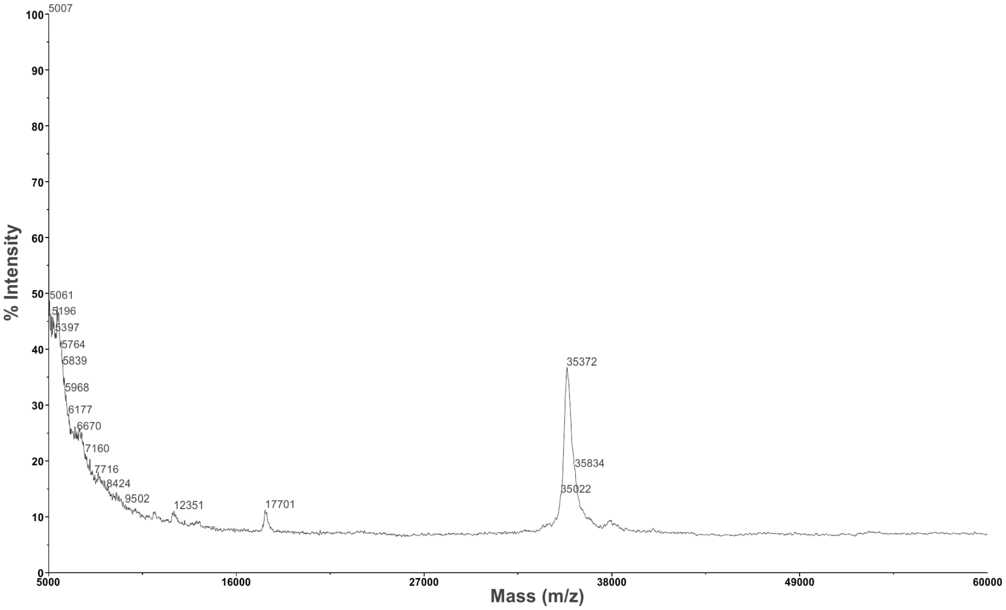

Figure S4: MALDI-ToF analysis of ***l*-P32**. The major peak corresponds to ***l*-P32** (m/z 35372, expected 35280). DCTB was used as matrix.

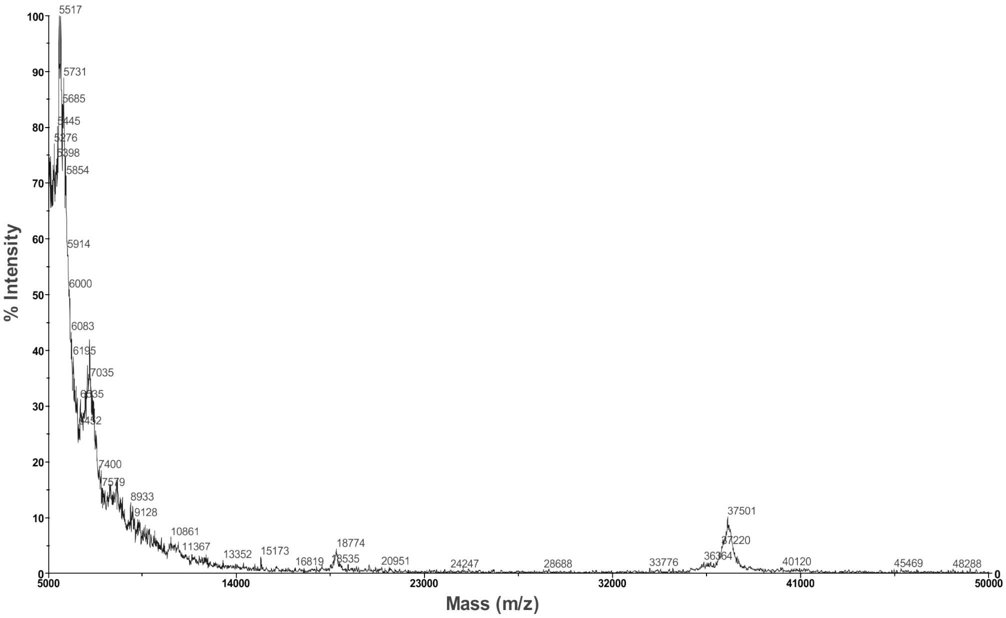

Figure S5: MALDI-ToF analysis of ***l*-P34**. The major peak corresponds to ***l*-P34** (m/z 37501, expected 37449.80). DCTB was used as matrix.

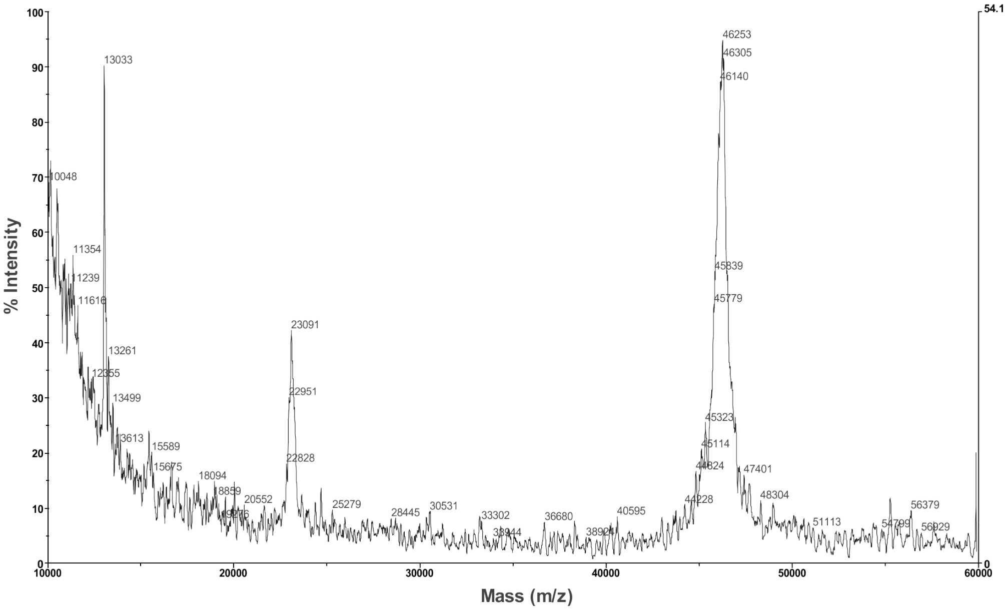

Figure S6: MALDI-ToF analysis of ***l*-P42**. The major peak corresponds to ***l*-P42** (m/z 46253, expected 46128.06). DCTB was used as matrix.

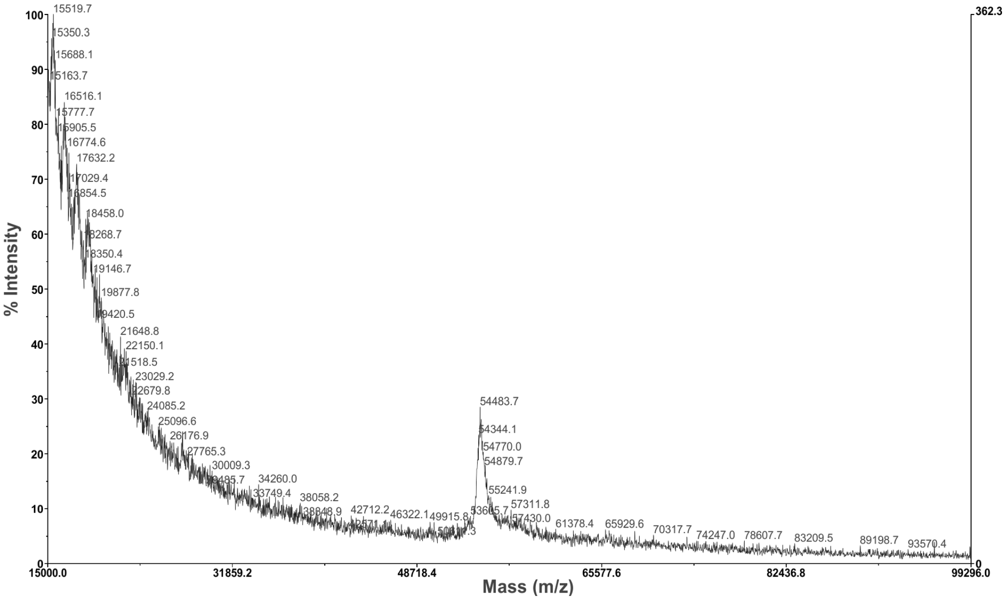

Figure S7: MALDI-ToF analysis of ***l*-P50**. The major peak corresponds to ***l*-P50** (m/z 54483.7, expected 54807.59). DCTB was used as matrix.

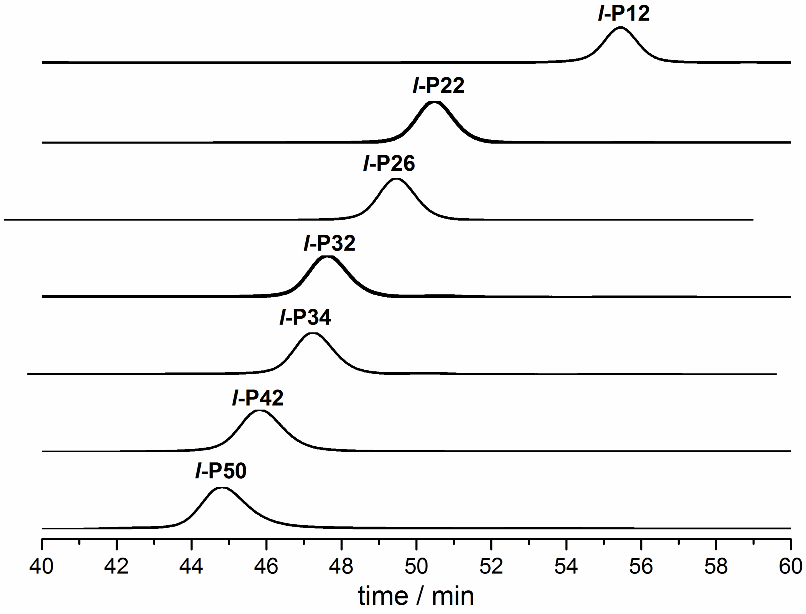

Figure S8: Analytical GPC traces (toluene/1% pyridine, detection at 500 nm) of all novel compounds ***l*-P12**, ***l*-P22**, ***l*-P26**, ***l*-P32**, ***l*-P34**, ***l*-P42** and ***l*-P50**.

S2 Steady-state photophysical characterization

Steady-state absorption and photoluminescence (PL) spectroscopy was carried out on dilute solutions (OD<0.1) of all molecules in toluene/1% pyridine (v/v%). Absorption measurements were performed using a Perkin-Elmer UV-Vis spectrophotometer. Normalized data are shown in Figure S9. All larger molecules have similar absorption spectrum, with a peak corresponding to a Q_x transition around 820 nm. Conversely, the smaller molecules (***c*-P6**, ***c*-P10** and ***l*-P6**) have relatively blueshifted spectra, due to a chain-length limited conjugation length. In particular, ***c*-P6** shows structure associated with vibronic coupling discussed in previous publications.[3]

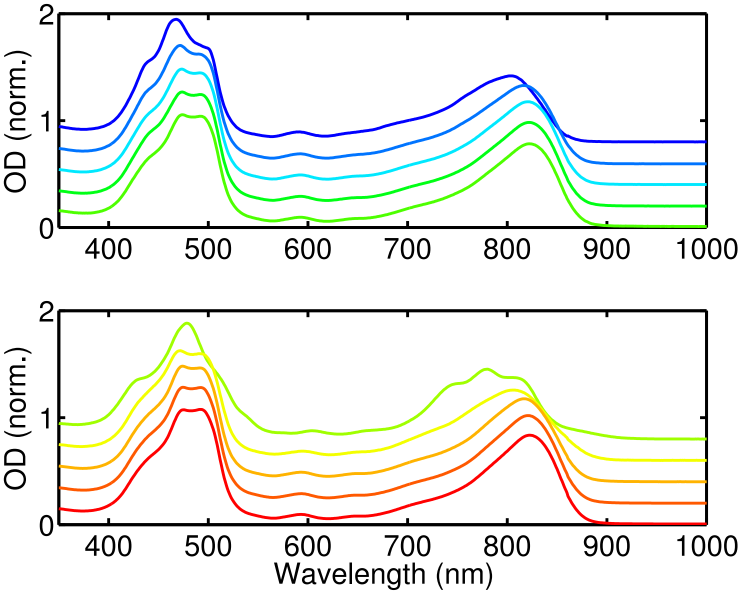

Figure S9: Normalized UV-Vis absorption spectra of all samples, offset for clarity. (Top panel) Linear oligomers from ***l*-P6** (upper, blue line), ***l*-P12**, ***l*-P22**, ***l*-P32** to ***l*-P42** (lower, green line). (Bottom panel) Nanorings, from ***c*-P6** (upper, green line), ***c*-P10**, ***c*-P20**, ***c*-P30** to ***c*-P40** (lower, red line).

Photoluminescence (PL) spectra were collected using the same experimental arrangement used for PL up-conversion. PL was measured after excitation with a low fluence (< 12 pJ/pulse) 750 nm (∼1.65 eV) ultrafast pulse of ∼100 fs duration. The emitted photons were spectrally filtered using a 780 nm long pass filter, with polarization selected parallel to the excitation polarization, and detected using a calibrated spectrometer with liquid-nitrogen cooled silicon CCD. Normalised PL spectra for each sample are shown in Figure S10. Larger molecules tended to emit around 860 nm, with a red (blue) shifted emission for the smaller nanorings (linear molecules), respectively. An exception is for ***c*-P6**; which shows strong Herzberg-Teller effects as discussed previously.[3]

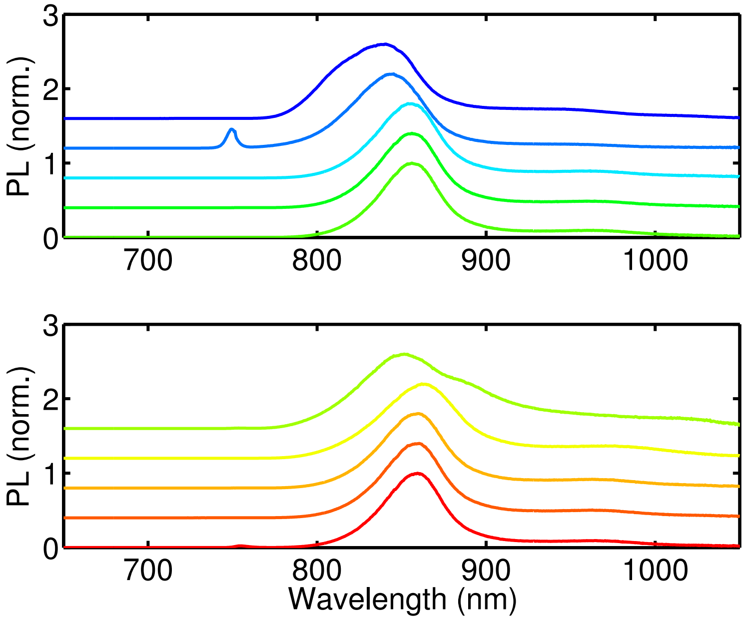

Figure S10: Normalized PL spectra of all samples following 750 nm excitation, offset for clarity. (Top panel) Linear oligomers from ***l*-P6** (upper, blue line), ***l*-P12**, ***l*-P22**, ***l*-P32** to ***l*-P42** (lower, green line). (Bottom panel) Nanorings, from ***c*-P6** (upper, green line), ***c*-P10**, ***c*-P20**, ***c*-P30** to ***c*-P40** (lower, red line). The spurious peak seen for ***l*-P12** originates from excitation laser scatter.

S3 Effective conjugation length

The exciton wavefunction extent within a molecule may be characterised by an 'effective conjugation length'. Such a measure is useful for interpreting dynamics and PL anisotropy (see below), and may be calculated using a number of techniques. Typically a fit to a plot of peak absorption energy against inverse number of repeat units is used, following the approach of either Meier[4] or Kuhn.[5] Manuscript Figure 1(d) shows the data for a wide range of linear porphyrin molecules, along with a Meier fit of the form

$$E_n = E_\infty + (E_1 - E_\infty)\mathrm{e}^{-a(n-1)}. \tag{1}$$

Here E_∞ represents the limiting value for $n \to \infty$ and E_1 is the value for the parent monomer ($n = 1$). The effective conjugation length is typically defined as the value of n for which no shift can be observed from the E_∞ value within the resolution of the spectrometer (typically within 1 nm). Fit values of $E_\infty = 1.509\,\mathrm{eV}$, $E_1 = 1.624\,\mathrm{eV}$ and $a = 0.2166$ give an effective conjugation length $n_{ecl} = 20$.

S4 Radiative and non-radiative recombination, and quantum efficiency measurements

The total recombination rate for excitons on the molecules under investigation may be measured using time-resolved PL techniques. While photoluminescence upconversion (used in the main manuscript) has excellent temporal resolution, it has limited dynamic range. Therefore, to measure the PL dynamics we used time-correlated single photon counting (TCSPC). The samples were excited using a 100 fs pulse of 750 nm wavelength radiation at low fluences, and emission was detected at the PL peak using a silicon single photon avalanche diode. This arrangement provided a temporal resolution of around 40 ps. The data for each sample (accompanied by a mono-exponential fit) are shown in Figure S11.

Quantum efficiency (also known as photoluminescence quantum yield) measurements were carried out using an integrating sphere technique. Briefly, photoexcitation at 450 nm using an LED source was used to excite a low concentration sample within an integrating sphere. PL was collected using a fibre coupled spectrometer; the system was calibrated using a black-body source of known emissivity. Quantum yield values were calculated using the procedure described in Reference 6. Final values were corrected by comparison to the ***l*-P6**

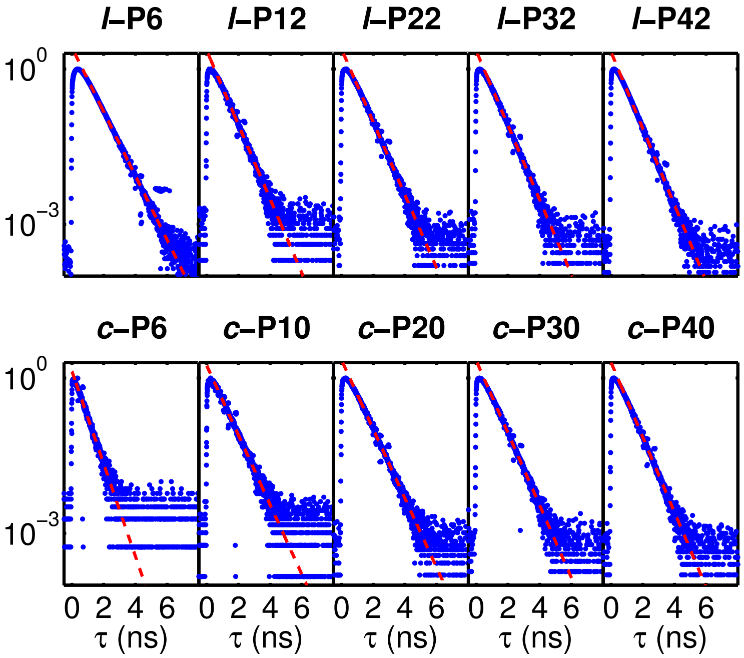

Figure S11: Time-resolved PL dynamics measured using TCSPC. Excitation was provided using 750 nm pulses, with detection at the peak PL wavelength for each sample. Dashed red lines are monoexponetial fits, with the values given in the text. Solvent used : 1% pyridine in toluene.

sample; the reference value of quantum efficiency for this molecule is 28%, calculated using multiple techniques and in comparison to multiple reference standards.[7] Figure S12 shows the measured values of quantum efficiency along with a representative error bar.

The radiative and non-radiative decay rates may be calculated from the total decay rate k_{tot} and the quantum efficiency (QE), using

$$k_{\text{rad}} = QE \times k \tag{2}$$

$$k_{\text{nr}} = k_{\text{tot}} - k_{\text{rad}} \tag{3}$$

The values for all samples are summarised in Figure S1.

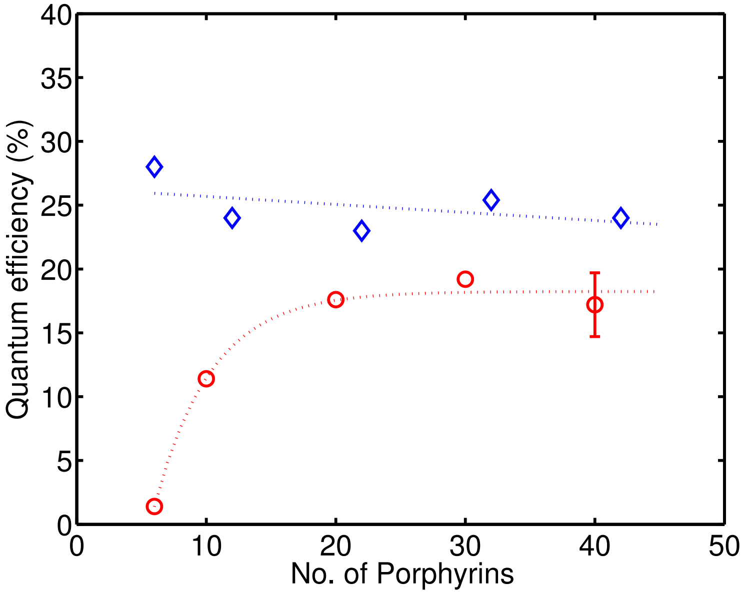

Figure S12: Quantum efficiency measured using an integrating sphere, under excitation into the Soret band (450 nm excitation). All data is referenced against ***l*-P6**, as described in the text. The errors bar represent uncertaintly for all data points; dashed lines are a guide to the eye. Solvent : 1% pyridine in toluene.

Table S1: Summary of total rate k_{tot}, radiative rate k_{rad}, non-radiative rate k_{nr} and quantum efficiency for all samples. Both radiative rate and non-radiative rate are calculated from total rate and quantum efficiency as described in the text.

Sample	k_{tot} (ns^{-1})	k_{rad} (ns^{-1})	k_{nr} (ns^{-1})	QY (% ± 2.5%)
***l*-P6**	1.43	0.399	1.03	28.0
***l*-P12**	1.65	0.396	1.25	24.0
***l*-P22**	1.62	0.373	1.25	23.0
***l*-P32**	1.66	0.421	1.24	25.4
***l*-P42**	1.70	0.408	1.29	24.0
***c*-P6**	2.06	0.029	2.03	1.4
***c*-P10**	1.55	0.176	1.37	11.4
***c*-P20**	1.54	0.271	1.27	17.6
***c*-P30**	1.61	0.309	1.30	19.2
***c*-P40**	1.67	0.287	1.38	17.2

S5 Photoluminescence up-conversion spectroscopy and anisotropy

Photoluminescence up-conversion (PLUC) was performed using an experimental arrangement described previously.[8] Briefly, a pulsed laser oscillator produced pulses of ~100 fs duration at 780 nm wavelength. Part of this pulse was used to photoexcite the sample with a fluence of approximately 125 pJ/pulse with a controllable polarization. This fluence was chosen to avoid excessive photodegredation effects or multiple exciton generation. The resultant PL was collected using off-axis parabolic mirrors, spectrally filtered using an 800 nm long pass filter, and focused upon a 1 mm thick θ=30°-cut BBO crystal in a motorised rotation mount. The remaining laser pulse was delayed using a mechanical translation stage and focused upon the crystal to gate the up-conversion process. The crystal was tuned to efficiently up-convert 860 nm PL. The up-converted photons were spatially and spectrally filtered to remove residual PL and self-doubled gate light using a 400 nm long-pass filter and a grating monochromator, before detection using a liquid-nitrogen cooled CCD.

Typical PLUC data are shown in Figure S13, after processing for averaging and removing a dark baseline. All transients exhibited a two-rate rise, empirically described using

$$\begin{aligned} PL(t) &= \qquad 0 && (t < 0) \\ &= A - B\exp\left(-t/\tau_1\right) - C\exp\left(t/\tau_2\right) && (t > 0) \end{aligned}$$

where A, B and C are constants between 0 and 1 and τ_1 and τ_2 are rise-times. The fast component (τ_1) represents the temporal response of the system, and corresponds to a half-width at half-maximum of around 230 fs. The second component is related to energy migration and relaxation of the molecule, and is more pronounced for the shorter linear chains due to mismatch between the peak emission and the chosen detection wavelength. This effect has been previously discussed in Reference 9. Data for ***c*-P6** exhibits a lower signal to noise (due to a forbidden lowest lying exciton state) and a slightly different dynamic, likely arising from the primarily Herzberg-Teller enabled luminescence.[3]

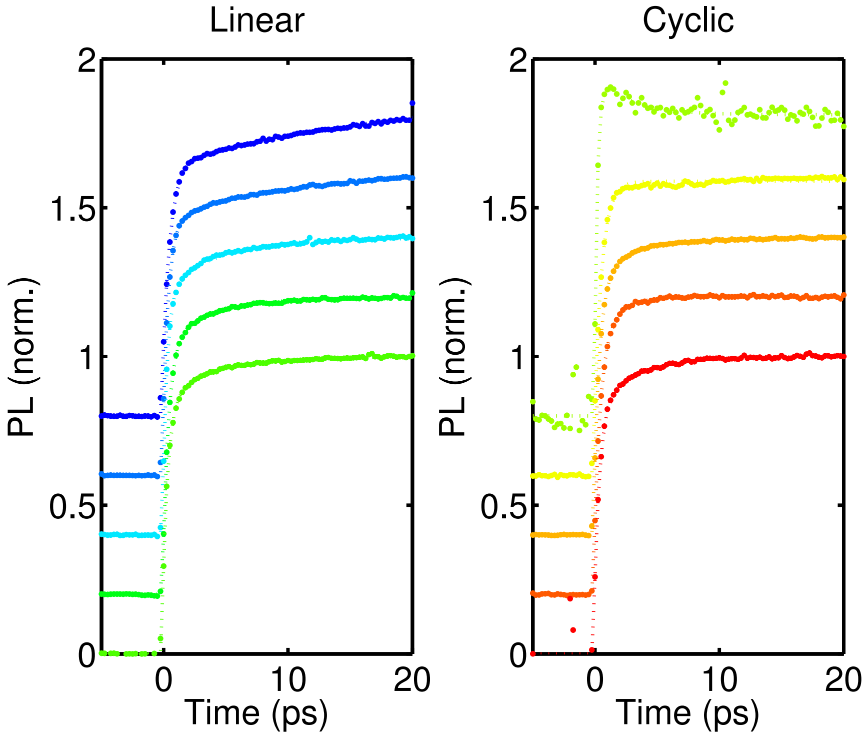

Figure S13: Typical normalized PLUC decays under excitation conditions used in the study (780 nm excitation, 125 pJ/pulse). (Left) The PLUC for the linear molecules from (top, blue) ***l*-P6** to (bottom, green) ***l*-P42**. (Right) The PLUC for cyclic molecules, from (top, green) ***c*-P6** to (bottom, red) ***c*-P40**. Two rise times can be seen – a fast component representing the temporal resolution of the system (around 230 fs HWHM), and a slower component related to energy migration and relaxation in the molecule.

S6 Molecular structural and exciton dynamics simulation

The PL anisotropy dynamics presented in the main text describe the electronic and geometrical environment experienced by the photoexcitations. A number of the features seen in the experimental data may be related to specific microscopic properties of the molecules, for instance:

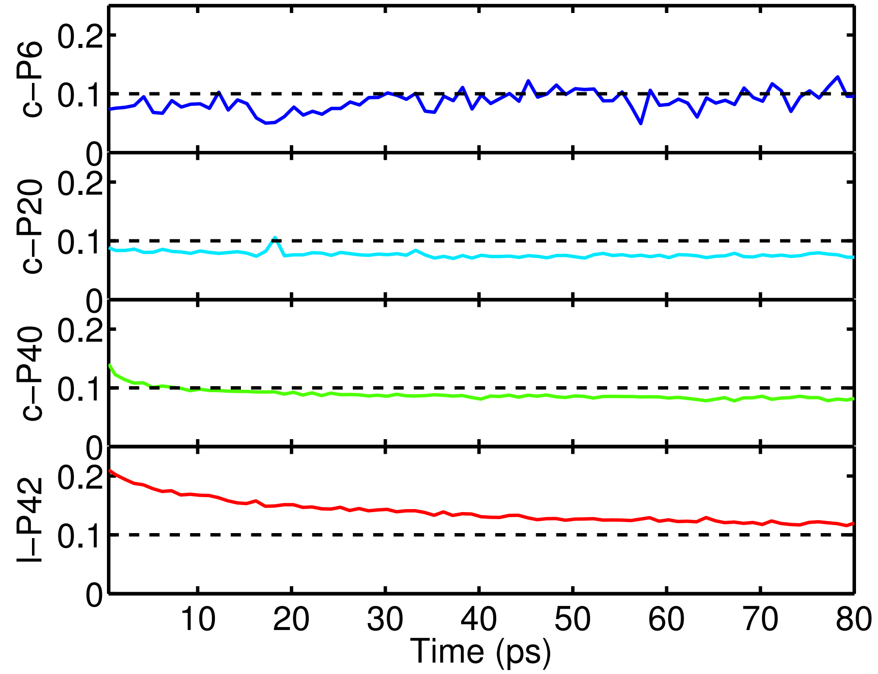

Figure S14: Time-resolved photoluminescence anisotropy for selected samples (top to bottom, ***c*-P6**, ***c*-P20**, ***c*-P40**, ***l*-P42**) over an extended time window. While all of the cyclic samples show a constant anisotropy over the 20 ps to 80 ps period, the linear molecule ***l*-P42** shows a continued drop arising from the conformations accessible to the linear topology.

Measured initial anisotropy is related to the size of the relaxed/self-trapped exciton. Such relaxation or self-trapping occurs on the order of the timescale of nuclear vibrations (10 fs) which cannot be resolved in the PLUC measurements. For linear oligomers, if the relaxed exciton is of the same size as the investigated molecule, little change between the dipole orientation of the initially excited and the relaxed exciton is expected and an initial anisotropy value of 0.4 is expected to be measured within the first 200 fs after excitation (the time-resolution of the system). When the investigated molecule size exceeds the relaxed exciton extent, reorientation is anticipated. A comparison of initial anisotropy with linear molecule size is therefore useful to provide an approximate measure of the relaxed exciton size. On the other hand, cyclic molecules that support complete delocalisation lead to an initial anisotropy value of 0.1 arising from the symmetry of the molecule; deviation from an initial anisotropy of 0.1 is a strong indication that the molecule does not support a delocalised exciton wavefunction.

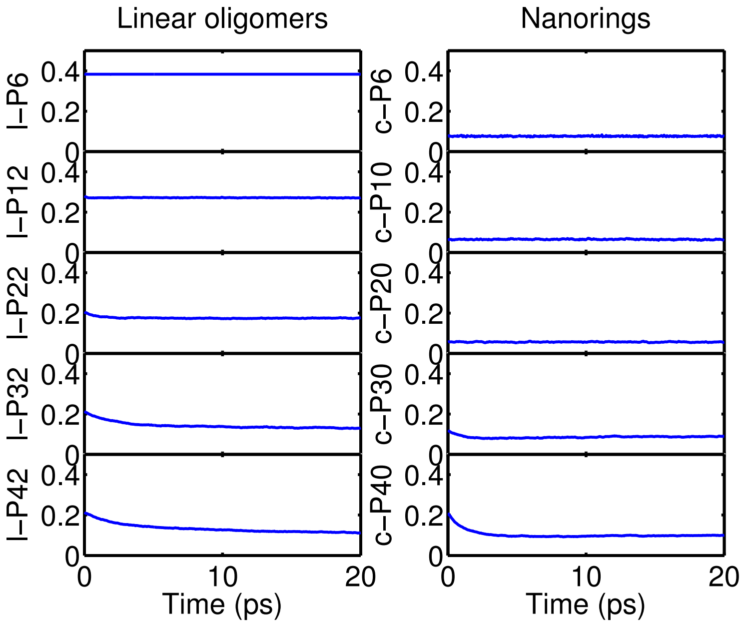

Figure S15: A complete set of exciton dynamics simulations are shown for all molecules studied for diffusion constant $D = 2\,\mathrm{units}^2/\mathrm{ps}$. Details of the simulation are given in the text.

Late-time anisotropy is related to the eventual reorientation of the emissive exciton from its initially excited position. There will be greatest reorientation possible for the longest and most disordered molecules; this value is a measure of the sub-dipole pointing distribution of the molecule.

Anisotropy dynamics provide information on the local curvature of the system. This is the least well defined parameters as a large number of microscopic features play into this measure, for instance, torsional relaxation, steric hinderance and on-chain disorder.

The PL anisotropy may be modelled by a quasi-classical hybrid approach used previously by Westenhoff and colleagues,[10,11] in which the structure of the molecule is first generated, and exciton dynamics are simulated on this static chain. This approach contains a number of simplifying assumptions; primarily that the chain may be assumed to be static (valid calculations in the solid-state) and that coherent effects may be neglected (reasonable on the picosecond timescale). We use two techniques to generate the molecular backbones for the simulation. In the linear case, a generator based upon a self-avoiding Monte-Carlo random walk is used with a self-exclusion radius of 0.7 nm corresponding to the diagonal size of a porphyrin unit. In the cyclic case, initially a basic chain is generated without disorder. Then, disorder is applied using the Metropolis Markov model suggested by Svatek *et al.*[12] The parameters used for this model were taken from Reference 12 as the same molecules are under investigation.

Exciton dynamics were then simulated on the generated backbone conformation. The following procedure is used:

Generate initial exciton An initial exciton of extent 20 units (or the chain length, whichever was smaller) was placed on the backbone and described using the line dipole model.[11,13] Sub-dipole units were chosen to correspond to single porphyrin repeat units for simplicity. The local amplitude of the exciton at each sub-dipole unit was calculated either using a sine-like exciton centre of mass (for the linear chains and nanorings larger than 20 units), or by uniformly distributing exciton amplitude (for nanorings smaller than 20 units). The transition dipole moment direction is calculated by summing the sub-dipole direction (given by the vector formed between the midpoints either side of the sub-unit) multiplied by the local exciton amplitude.

Relax the exciton For linear chains, the exciton was immediately 'collapsed', reducing its extent to 6 units centred randomly within the initially generated exciton wavefunction. Following this step, the local exciton wavefunction amplitude was calculated as above using the sine-like centre of mass for linear chains and nanorings larger than 6 units. For cyclic molecules of less than 10 units, complete delocalisation is used as we have previously shown for ***c*-P6**.[3] The new transition dipole moment is calculated, and the difference between these provides an intial anisotropy using the equation given in the main manuscript.

Exciton diffusion On-chain exciton motion is widely studied and typically requires a high level of quantum chemical calculation. For this reason, a simple one-dimensional diffusion model is used with a diffusion constant that is determined by a global fit to the experimental results. In each timestep (50 fs) the exciton moves a distance picked from a normal distribution with close to unit standard deviation. At each timestep, a new anisotropy value is calculated.

By repeating the exciton simulation procedure 50 times for each chain conformation, and generating each conformation 300 times, an ensemble average of the anisotropy dynamics may be built up. The simulated anisotropy is shown for all molecules in Figure S15, key cases are shown in the main text for ***l*-P42**, ***c*-P6**, ***c*-P20** and ***c*-P40**.

In addition to obtaining the initial exciton size through Meier modelling of the absorption, it is fruitful to consider the quality of the fit between the simulation and the experimental data. Figure S16 shows the variation of the quality of the agreement (using an initial residual) as a function of exciton size, which indicates an initial exciton size of 15 - 20 provides the best fit, in agreement with the value of 20 units found using the Meier approach.

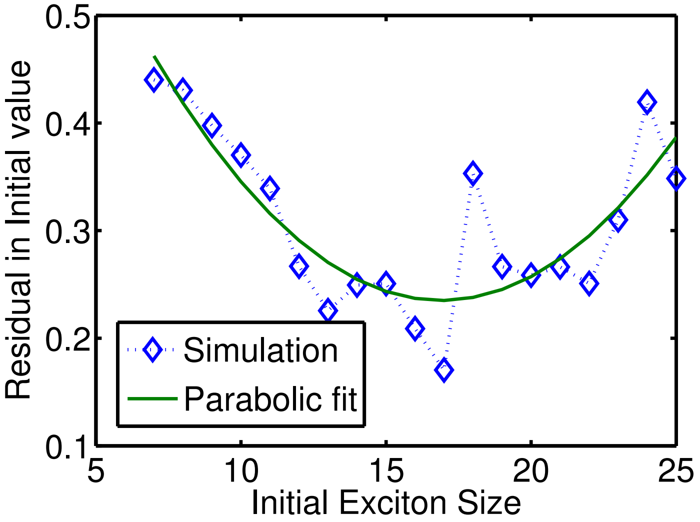

Figure S16: The dependence of the initial residual (sum of the difference between the simulated and experimental initial anisotropy for all samples) as a function of the initial exciton size in the simulation.

In the Kasha model,[14,15] the dipole strength can be conceptually likened to a vector summation over sub-dipoles. By summing over the sub-dipoles in the simulation using

$$d = \left| \sum_i a_i \widehat{\phi_i} \right| \tag{4}$$

where a_i is the amplitude prefactor for the sub-dipole and $\widehat{\phi_i}$ is the direction of the sub-dipole, a value related to dipole strength (d) may be calculated using a values for relax excitons. Figure S17 shows a comparison between the simulated dipole strength and experimentally determined radiative rate, revealing a qualitatively similar behaviour of radiative rate with topology and molecule size. It should be noted that in the simulation, the linear and cyclic structures tend to the same asymptote; this indicates that the origin of the deviation seen in the experimental data does not arise from a purely topological effect and likely comes from a structural cause.

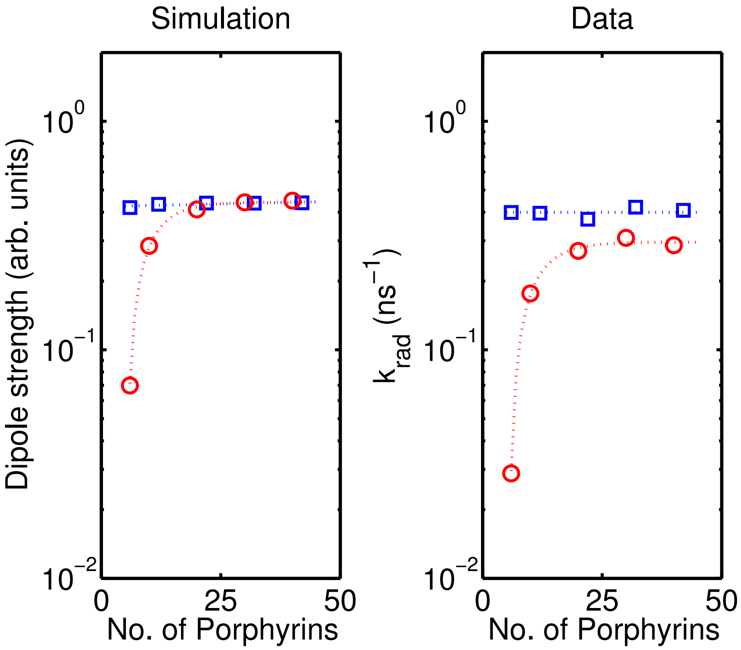

Figure S17: (Left) Simulated dipole strength and (Right) experimentally measured radiative rate as a function of topology and molecule size. Data for the linear molecules are shown as open blue squares, while cyclic molecule are shown as open red circles. Dashed lines are a guide to the eye.

References

(1) Wilkinson, J. D.; Wicks, G.; Nowak-krol, A.; Lukasiewicz, L. G.; Wilson, C. J.; Drobizhev, M.; Rebane, A.; Gryko, D. T.; Anderson, H. L. *J. Mater. Chem. C* **2014**, *2*, 6802–6809.

(2) Kondratuk, D. V.; Perdigão, L. M. A.; Esmail, A. M. S.; O'Shea, J. N.; Beton, P. H.; Anderson, H. L. In Review.

(3) Sprafke, J. K. et al. *J. Am. Chem. Soc.* **2011**, *133*, 17262–17273.

(4) Meier, H.; Stalmach, U.; Kolshorn, H. *Acta Polym.* **1997**, *48*, 379–384.

(5) Kuhn, W. *Helv. Chim. Acta* **1948**, *31*, 1780–1799.

(6) Mello, J. C. D.; Wittmann, H. F.; Friend, R. H. *Adv. Mater.* **1997**, *9*, 230.

(7) Yong, C. K. et al. *Chemical Science* **2015**, DOI: 10.1039/C4SC02424A.

(8) Parkinson, P.; Knappke, C. E. I.; Kamonsutthipaijit, N.; Sirithip, K.; Matichak, J. D.; Anderson, H. L.; Herz, L. M. *J. Am. Chem. Soc.* **2014**, *136*, 8217–8220.

(9) Chang, M. H.; Hoffmann, M.; Anderson, H. L.; Herz, L. M. *J. Am. Chem. Soc.* **2008**, *130*, 10171–10178.

(10) Westenhoff, S.; Daniel, C.; Friend, R. H.; Silva, C.; Sundström, V.; Yartsev, A. *J. Chem. Phys.* **2005**, *122*, 094903.

(11) Westenhoff, S.; Beenken, W. J. D.; Yartsev, A.; Greenham, N. C. *J. Chem. Phys.* **2006**, *125*, 154903.

(12) Svatek, S. A.; Perdigao, L. M. A.; Stannard, A.; Wieland, M. B.; Kondratuk, D. V.; Anderson, H. L.; O'Shea, J. N.; Beton, P. H. *Nano Lett.* **2013**, *13*, 3391–3395.

(13) Beenken, W. J. D.; Pullerits, T. *J. Chem. Phys.* **2004**, *120*, 2490.

(14) Kasha, M.; Rawls, H. R.; Ashraf El Bayoumi, M. *Pure Appl. Chem.* **1965**, *11*, 371–392.

(15) Kasha, M. *Radiat. Res.* **1963**, *20*, 55.